

See discussions, stats, and author profiles for this publication at: <https://www.researchgate.net/publication/226825188>

# Theoretical investigation of photoelectron spectra and magnetically induced current densities in ring-shaped transition-metal oxides

ARTICLE in THEORETICAL CHEMISTRY ACCOUNTS · JUNE 2011

Impact Factor: 2.23 · DOI: 10.1007/s00214-011-0946-4

CITATIONS

6

READS

23

## 5 AUTHORS, INCLUDING:



Heike Fliegl

University of Oslo

36 PUBLICATIONS 846 CITATIONS

SEE PROFILE



Chan Ying

Ashland Community Hospital

99 PUBLICATIONS 1,762 CITATIONS

SEE PROFILE



Michael Patzschke

University of Helsinki

27 PUBLICATIONS 577 CITATIONS

SEE PROFILE



Dage Sundholm

University of Helsinki

205 PUBLICATIONS 4,615 CITATIONS

SEE PROFILE

# Theoretical investigation of photoelectron spectra and magnetically induced current densities in ring-shaped transition-metal oxides

Heike Fliegl · Olli Lehtonen · Ying-Chan Lin ·  
Michael Patzschke · Dage Sundholm

Received: 28 March 2011 / Accepted: 16 April 2011 / Published online: 4 May 2011  
© Springer-Verlag 2011

**Abstract** The molecular structures of cyclic group 6 transition-metal ( $M = \text{Cr, Mo, W, Sg}$ ) oxides ( $M_3O_9^{0/1-2-}$ ) species have been optimized at density functional theory (DFT) levels. The photoelectron spectra (PES) of  $M_3O_9^-$  ( $M = \text{Cr, Mo, W}$ ) were calculated at the time-dependent DFT and approximate coupled-cluster singles doubles (CC2) levels and compared with experimental results. The CC2 calculations did not yield any reliable PES, whereas the molecular structures can be identified by comparing PES obtained at the DFT level with experiment. Magnetically induced current densities were calculated at the DFT level using the gauge-including magnetically induced current (GIMIC) approach. The current strengths and current pathways of the neutral  $M_3O_9$  and the dianionic  $M_3O_9^{2-}$

( $M = \text{Cr, Mo}$ ) oxides were investigated and analyzed with respect to a previous prediction of  $d$ -orbital aromaticity for  $Mo_3O_9$  anions. Current-density calculations provide ring-current strengths that are used to assess the degree of aromaticity. Comparison of current-density calculations and calculations of nucleus-independent chemical shifts (NICS) shows that NICS calculations are not a reliable tool for determining the degree of aromaticity of the metal oxides.

**Keywords** Photoelectron spectra · Magnetically induced current · Aromaticity

Dedicated to Professor Pekka Pyykkö on the occasion of his 70th birthday and published as part of the Pyykkö Festschrift Issue.

**Electronic supplementary material** The online version of this article (doi:10.1007/s00214-011-0946-4) contains supplementary material, which is available to authorized users.

H. Fliegl (✉) · O. Lehtonen · M. Patzschke · D. Sundholm  
Department of Chemistry, University of Helsinki,  
POB 55 (A.I. Virtanens plats 1), 00014 Helsinki, Finland  
e-mail: Heike.Fliegl@helsinki.fi

O. Lehtonen  
e-mail: Olli.Lehtonen@helsinki.fi

M. Patzschke  
e-mail: Michael.Patzschke@helsinki.fi

D. Sundholm  
e-mail: Dage.Sundholm@helsinki.fi

Y.-C. Lin  
Department of Chemistry, Center for Theoretical  
and Computational Chemistry, University of Tromsø,  
9037 Tromsø, Norway  
e-mail: Ying-Chan.Lin@uit.no

## 1 Introduction

The molecular and electronic structure as well as the chemical bonding of small clusters of chromium, molybdenum, and tungsten oxides have recently been investigated by employing computational and experimental methods [1–15]. The cluster structures were identified by measuring the photoelectron spectra (PES) of the metal oxides in molecular-beam experiments. The electronic structure and chemical-bonding properties were studied by comparing measured PES with electronic detachment energies calculated at density functional theory and *ab initio* correlation levels. These and other studies on small metal-oxide clusters have recently been reviewed [16].

Metal-oxide clusters have awakened interest because they can be used as model systems to understand the reaction mechanisms of metal-oxide catalysts [4, 17]. The computational studies of metal-oxide clusters show that ring-shaped structures possess an extraordinary energetic stabilization. King suggested 20 years ago that the stabilization of the metal-oxide rings was due to aromaticity of

the O–M–O bonds [18]. More recently, Wang et al. suggested that the aromatic stabilization of the  $M_3O_9^{1-/2-}$  clusters actually involves the d electrons giving rise to the so called *d*-orbital aromaticity [1]. The computational study by Huang et al. showed that negatively charged  $M_3O_9$  clusters have fully delocalized metal–metal bonds, the d orbitals of which form an aromatic  $\sigma$  bond [1].

The *d*-orbital aromaticity concept was actually introduced by Wannere et al. who suggested somewhat earlier that coinage-metal four-membered rings are d-orbital aromatic [19], a notion that was questioned by Lin et al. [20]. The *d*-orbital aromaticity was further extended by Zhai et al. who found in a combined experimental and computational study that  $Ta_3O_3^-$  possesses a double *d*-orbital aromaticity involving both  $\pi$  and  $\delta$  orbitals [5]. Based on extensive computational studies on a  $Hf_3$  ring, Averkiev and Boldyrev generalized the *d*-orbital aromaticity concept to triple,  $\sigma$ ,  $\pi$ , and  $\delta$  aromaticity involving the d orbitals [12].

The metal aromaticity concept is a generalization of aromaticity originally intended for cyclic hydrocarbons. The first experimental evidences for aromatic and antiaromatic metal clusters were found in  $Al_4^{2-/4-}$  rings [21–23]. The doubly  $\sigma$  aromaticity and  $\pi$  antiaromaticity of the  $Al_4^{4-}$  ring was later questioned [24, 25]. The existence of metal antiaromaticity was debated in Chemical Engineering News without reaching any consensus [26]. Lin et al. studied the magnetically induced current densities of the  $Al_4^{2-/4-}$  rings using their gauge-including magnetically induced current (GIMIC) method [27, 28]. They found that  $Al_4^{2-}$  sustains diatropic currents in the molecular plane. Ring-current contributions were also obtained at longer distances from the molecular plane. The current calculations propose that according to the ring-current criterion  $Al_4^{2-}$  is mainly  $\sigma$  aromatic though with a significant ring-current contribution from the  $\pi$  region. The  $Al_4^{4-}$  ring was found to possess a strong diatropic current transported by the  $\sigma$  electrons, but an equally strong paratropic current was found to circle around the ring in the  $\pi$  orbitals above and below the  $Al_4^{4-}$  ring [27]. Thus, the GIMIC calculations seemed to support the notion that  $Al_4^{4-}$  is simultaneously aromatic and antiaromatic [23]. However, the net ring-current strength is very small, which would rather suggest that  $Al_4^{4-}$  is nonaromatic. Ring-current calculations on cyclic nonaromatic hydrocarbons show that they indeed sustain spatially separated diatropic and paratropic ring-currents of the same strengths that cancel [29]. The analogy to the hydrocarbons would suggest that  $Al_4^{4-}$  is nonaromatic even though it sustains strong diatropic and paratropic ring currents. Islas *et al.* also found that  $Al_4^{4-}$  has a diatropic  $\sigma$ -system and a paratropic  $\pi$ -system and may thus be called “bitropic” [30].

The GIMIC method has proven to be a very useful tool for assessing different kinds of molecular aromaticity

according to the ring-current criterion [31–40]. Integration of the current-density strength circling around the molecular rings yields a measure of the degree of aromaticity. Current strengths at selected bonds in combination with current-density plots reveal the current-flow pathways in multi-ring systems.

Here, we investigate the aromatic properties of the closed-shell  $M_3O_9^{0/2-}$  ( $M = Cr, Mo$ ) rings by calculating the magnetically induced current density. The aromatic character is also investigated by nuclear-independent chemical shift calculations at the ring center [41] and by calculating the nuclear magnetic shielding function in discrete points along the symmetry axis of the molecular rings [42, 43]. The molecular and electronic structures are assessed by calculating the PES at ab initio electron correlation and density functional theory levels. The obtained PES are compared with previously calculated electron detachment energies and with measured spectra.

The computational methods are described in Sect. 2, and the results are presented in Sect. 3. The molecular and electronic structures are discussed in Sects. 3.1 and 3.2, respectively. The calculated electron detachment energies and the corresponding PES are compared with experiment in Sect. 3.3. The aromatic character of the investigated molecules deduced from nuclear magnetic shielding functions are discussed in Sect. 3.4. Calculations of magnetically induced current densities and determination of the degree of molecular aromaticity according to the magnetic ring-current criterion are presented in Sect. 3.5. In Sect. 4, we summarize and discuss the main results of this work.

## 2 Computational methods

The molecular structures were optimized at the density functional theory (DFT) level using TURBOMOLE [44]. The TPSS functional [45] and the def2-TZVPP basis set [46] were employed, as the TPSS functional has been found to work well for elements in the whole periodic table [47] and the def2-TZVPP basis sets yield structures close to the basis-set limit. In the structure optimization, the core electrons of Mo and W were considered by the corresponding effective core potentials (ECP) [48]. The optimized structures were confirmed to be minima by evaluating structural force constants. Neutral and dianionic species were checked for singlet and triplet instabilities with the PBE functional [49], because instability calculations using the TPSS functional were not feasible. The dianions were additionally optimized with neutralizing point charges of +1 placed 20 a.u. above and below the center of molecular ring, followed by a force constant calculation. The changes in geometries were small ( $\leq 0.01$

Å), and the ground-state point group was not affected by the point charges.

Further optimizations were done using the Amsterdam Density Functional (ADF) program [50–52]. Here, the ADF triple- $\zeta$  polarization (TZ2P) basis sets were used together with a small frozen core. The BP86 functional [53–55] was employed in all ADF calculations. The relativistic calculations were done with the scalar zeroth-order regular approximation (ZORA) and the spin-orbit ZORA methods [56]. Force constants were calculated for all optimized structures to confirm that they represent minima on the potential energy surface. As the TURBOMOLE calculations showed no significant change upon inclusion of point charges for the dianion, this method was not employed in the ADF calculations. The ZORA calculations were done only for the tungsten and seaborgium (Sg) compounds, where relativistic effects are considerable.

The photodetachment energies were computed at the DFT and the approximate coupled-cluster singles and doubles (CC2) [57–59] levels. The DFT calculations were performed using the B3LYP [60, 61] functional and the Karlsruhe triple- $\zeta$  def2-TZVPP basis sets together with the Stuttgart effective core potentials (ECP) for Mo and W [48]. The core electrons were considered in all calculations on the chromium species. The first vertical detachment energy (VDE) of the anions were calculated as the energy difference between the anion and the neutral cluster using the molecular structure of the anion, whereas the first adiabatic detachment energy (ADE) is obtained using the fully optimized structure of both the anion and the neutral molecule. The low-energy part of the PES of the singly charged anions can be simulated by adding calculated vertical singlet and triplet excitation energies of the neutral molecule to the first VDE, thus assuming that the anion has a doublet ground-state.

The CC2 photoelectron spectra for  $\text{Mo}_3\text{O}_9^-$  and  $\text{W}_3\text{O}_9^-$  were obtained by adding CC2 excitation energies to the first VDE calculated at the Hartree-Fock self-consistent field (HF SCF) level. For  $\text{Cr}_3\text{O}_9^-$ , the CC2 calculation did not converge due to the large multi-reference character of the wave function. The CC2 singlet and triplet excitation energies were calculated with TURBOMOLE using the RICC2 module [58, 59]. The def2-TZVPP basis sets and the resolution of the identity approximation were employed in the CC2 calculations [46, 62].

The PES were also obtained at the B3LYP level by adding singlet and triplet excitation energies to the first VDE calculated as the energy difference between the anion and the neutral molecule. The first VDE was calculated at the DFT level, whereas the excitation energies were obtained using time-dependent density functional theory (TD-DFT) calculations employing the ESCF module of the TURBOMOLE program package [63, 64].

The DGrid 4.5 program [65] was used to calculate electron densities and electron-localization indicator distributions (ELI-D) [66]. The ELI-D was then subjected to a basin analysis. The electron density was integrated over these basins to evaluate the number of electrons inside them.

Nuclear magnetic shielding tensors were calculated at the B3LYP level [60, 61] using TURBOMOLE [67–69]. Nuclear magnetic resonance (NMR) shielding constants and ring-current susceptibilities, yielding the ring-current strengths for a given value of the external magnetic field, were calculated for  $\text{Cr}_3\text{O}_9$  and  $\text{Cr}_3\text{O}_9^{2-}$  using the B3LYP functional and the def2-TZVPP basis sets. In the NMR shielding calculations on  $\text{Mo}_3\text{O}_9$  and  $\text{Mo}_3\text{O}_9^{2-}$ , a triple- $\zeta$  all-electron basis set (TZVPPalls2) was used for Mo and the def2-TZVPP basis set was used for O [70]. Magnetic shielding calculations could not be performed on the W and Sg compounds nor for the open-shell anions.

The magnetically induced current densities were calculated at the same level as the nuclear magnetic shielding tensors using the GIMIC method. GIMIC is an independent program that uses basis-set information as well as the magnetically perturbed and unperturbed density matrices from nuclear magnetic shielding calculations as input data [28]. Explicit values for current susceptibilities can be obtained by numerical integration of the current density passing through cut planes perpendicularly to selected bonds of the molecular system [28]. The ring-current susceptibility, denoted in the following as ring-current strength, can be used as a reliable measure of the molecular aromaticity. The current strengths in combination with current-density plots provide detailed information about the current pathway in molecules. The ring-current strength (susceptibility) of 11.8 nA/T for benzene calculated at the B3LYP/def2-TZVPP level can be used as reference value for typically aromatic molecules [29]. The sign and magnitude of the obtained ring-current strengths indicate whether molecular rings are aromatic, antiaromatic, or nonaromatic thus having diatropic, paratropic, or vanishing net ring current, respectively [29].

### 3 Results and discussion

#### 3.1 Molecular structures

The ground-state of  $\text{Cr}_3\text{O}_9$  is a singlet  $^1\text{A}_1$  state with a nonplanar structure of  $\text{C}_{3v}$  symmetry. The lengths of the Cr=O double bonds are 1.573 and 1.576 Å and the Cr–O single bonds are 1.775 Å long. The  $\text{Cr}_3\text{O}_9^-$  anion exhibits Jahn-Teller distortion [3]. Its ground-state structure has  $\text{C}_s$  symmetry and the lowest electronic state is  $^2\text{A}'$ , which agrees with the previous study by Zhai et al. [3]. For the

anion, the lengths of the Cr=O bonds are 1.593, 1.595, and 1.598 Å. The lengths of the Cr–O bonds are 1.817, 1.733, and 1.784 Å. The ground-state of  $\text{Cr}_3\text{O}_9^{2-}$  is a singlet  $^1A_1'$  state with a planar structure of  $D_{3h}$  symmetry. The lengths of the Cr=O and Cr–O bonds of the dianion are 1.617 Å and 1.792 Å, respectively. The lower  $C_{3v}$  symmetry obtained for  $\text{Cr}_3\text{O}_9$  might be due to the multi-reference character of the ground-state wave function as discussed in Sect. 3.3.

The ground-state of  $\text{Mo}_3\text{O}_9$  is a singlet  $^1A_1'$  state with a planar structure of  $D_{3h}$  symmetry. The length of the Mo=O bonds is 1.693 Å and the Mo–O distances are 1.900 Å. The  $\text{Mo}_3\text{O}_9^-$  anion exhibits Jahn-Teller distortion. Its has a  $^2A_1$  ground-state with  $C_{2v}$  symmetry. The lengths of the Mo=O bonds are 1.716 and 1.722 Å and Mo–O single bonds are 1.952, 1.851, and 1.914 Å long. The ground-state of the  $\text{Mo}_3\text{O}_9^{2-}$  dianion is  $^1A_1'$  of  $D_{3h}$  symmetry. The Mo=O and Mo–O bond lengths of the dianion are 1.739 and 1.920 Å, respectively.

At the TPSS level, the tungsten oxides have the same ground-state structures and symmetries as the corresponding molybdenum compounds. For neutral  $\text{W}_3\text{O}_9$ , the lengths of the W=O and W–O bonds are 1.718 and 1.911 Å, respectively. The Jahn-Teller distorted  $\text{W}_3\text{O}_9^-$  has W=O distances of 1.739 and 1.741 Å. The lengths of the W–O bonds are 1.996, 1.852, and 1.922 Å. For the  $\text{W}_3\text{O}_9^{2-}$  dianion, the lengths of the W=O and W–O bonds are 1.759 and 1.935 Å, respectively. The molecular and electronic structures for the Mo and W clusters agree with those obtained by Li and Dixon [71]. It should be noted, however, that the metal oxides are very floppy. At the BP86 level, the  $D_{3h}$  structure of the  $\text{W}_3\text{O}_9^-$  anion is 23 kJ/mol below the Jahn-Teller distorted  $C_{2v}$  structure. Spin-orbit coupling has a very small influence on the structure of the tungsten compounds. For the lighter metal oxides, spin-orbit effects are expected to be even smaller. For all optimized species, the biggest change in the bond distances due to spin-orbit effects is 0.2 Å and the bond angles change by less than 0.3°. The molecular structures obtained at the BP86 level using ADF are in excellent agreement with those calculated with TURBOMOLE.

For neutral  $\text{Sg}_3\text{O}_9$  ( $D_{3h}$ ), the length of the Sg=O bonds is 1.788 Å at the scalar ZORA level and 1.784 Å at the spin-orbit ZORA level. The lengths of the corresponding Sg–O bonds are 1.977 and 1.968 Å, respectively. For the anion, the  $D_{3h}$  structure is also lowest in energy. The doublet is lower than the quartet by almost 500 kJ/mol. For the doublet state of the anion, the Sg=O bonds were found to be 1.805 Å (scalar) and 1.799 Å (spin-orbit) long. The lengths of Sg–O bonds are 1.997 Å (scalar) and 1.990 Å (spin-orbit). The dianion has a singlet ground-state of  $D_{3h}$  symmetry. For the dianion, the Sg=O bond lengths of 1.827 Å (scalar) and 1.821 Å (spin-orbit) were obtained, while the Sg–O bonds are 2.005 Å (scalar) and 1.999 Å (spin-

orbit) long. Spin-orbit effects are very small even for the transactinide seaborgium compounds. No transactinide break [72] could be detected. Judged from the properties of the  $\text{Sg}_3\text{O}_9^{0/1-2-}$  species, seaborgium is a normal member of group 6 in the periodic table.

The bond lengths and bond angles calculated at different levels of theory for neutral  $\text{Cr}_3\text{O}_9$ ,  $\text{Mo}_3\text{O}_9$ , and  $\text{W}_3\text{O}_9$  are compared in tables given as supplementary material. Cartesian coordinates of the studied species can also be found in the supplementary material. Selected bond lengths and bond angles obtained in nonrelativistic calculations as well as in relativistic calculations using ECPs and all-electron scalar and spin-orbit relativistic Hamiltonians are given in Tables 1 and 2. The benchmark calculations using different basis sets show that def2-TZVPP yields molecular structures close to the basis-set limit, whereas the bond distances and bond angles obtained using the def2-SVP basis set deviate typically by  $\pm 0.01$  Å and  $1^\circ$  from the def2-TZVPP ones. Hybrid functionals and the SVWN functional at the local density approximation tend to give somewhat shorter bond distances than the ones obtained using functionals at the generalized gradient approximation. Comparison of the molecular structures for  $\text{Mo}_3\text{O}_9$  obtained in the all-electron calculations with the values obtained in scalar-relativistic ECP calculations shows that relativistic effects slightly decrease its bond lengths.

### 3.2 Electronic structure

The electronic structure calculations on the neutral  $\text{M}_3\text{O}_9$  molecules show that the lowest unoccupied molecular orbital (LUMO) is located between the metal atoms inside the metal-oxide ring as also obtained in previous studies [1, 2]. Density differences between the neutral, anionic, and dianionic  $\text{M}_3\text{O}_9$  were calculated using the molecular structure of the dianionic species. The density-difference

**Table 1** M–O and M–M bond lengths (R and M–M in Å) as well as O–M–O angles (A in degrees) for neutral, anionic, and dianionic  $\text{Cr}_3\text{O}_9$ ,  $\text{Mo}_3\text{O}_9$  and  $\text{W}_3\text{O}_9$  obtained at the TPSS/def2-TZVPP level

	R	M–M	A
$\text{Cr}_3\text{O}_9$ ( $D_{3h}$ )	1.775	3.088	104.0
$\text{Cr}_3\text{O}_9^-$ ( $C_s$ )	1.784/1.733/1.817	3.131/3.224	104.8/94.4
$\text{Cr}_3\text{O}_9^{2-}$ ( $D_{3h}$ )	1.792	2.940	129.8
$\text{Mo}_3\text{O}_9$ ( $D_{3h}$ )	1.900	3.519	104.3
$\text{Mo}_3\text{O}_9^-$ ( $C_{2v}$ )	1.914/1.851/1.952	3.433/3.659	104.6/86.8
$\text{Mo}_3\text{O}_9^{2-}$ ( $C_{2v}$ )	1.936/1.854/1.940	3.331/3.692	107.4/79.6
$\text{Mo}_3\text{O}_9^{2-}$ ( $D_{3h}$ )	1.920	3.072	133.8
$\text{W}_3\text{O}_9$ ( $D_{3h}$ )	1.911	3.536	104.6
$\text{W}_3\text{O}_9^-$ ( $C_{2v}$ )	1.922/1.852/1.996	3.415/3.727	105.1/82.3
$\text{W}_3\text{O}_9^{2-}$ ( $D_{3h}$ )	1.935	3.061	135.5



**Table 2** W–O and Sg–O bond lengths (R in Å) as well as metal to metal distances M–M and O–W–O and O–Sg–O angles (A in degrees) for neutral, anionic, and dianionic  $W_3O_9$  and  $Sg_3O_9$  obtained at the BP86/TZ2P level using the scalar-relativistic correction ZORA method (SC) and ZORA including spin-orbit coupling (SO)

	Method	R	M–M	A
$W_3O_9$	SO	1.903	3.513	105.3
( $D_{3h}$ )	SC	1.906	3.514	105.6
$W_3O_9^-$	SO	1.973/1.853/1.917	3.410/3.695	84.1/105.3
( $C_{2v}$ )	SC	1.981/1.852/1.920	3.397/3.706	83.1/105.8
$W_3O_9^{2-}$	SO	1.923	3.229/3.227	125.9
( $D_{3h}$ )	SC	1.925	3.233	125.8
$W_3O_9^{2-}$	SO	1.930	3.053	135.4
( $D_{3h}$ )	SC	1.931	3.055	135.5
$Sg_3O_9$	SO	1.968	3.599	107.8
( $D_{3h}$ )	SC	1.978	3.607	108.0
$Sg_3O_9^-$	SO	1.990	3.284	128.8
( $D_{3h}$ )	SC	1.997	3.313	127.9
$Sg_3O_9^{2-}$	SO	1.999	3.132	136.9
( $D_{3h}$ )	SC	2.005	3.148	136.5

plots and electron localizability indicator distributions (ELI-D) are given as supplementary material. Plots of density differences between the neutral and dianionic species and the ELI-D function for  $Mo_3O_9^{2-}$  are given in Fig. 1. The figure shows that the reduction in the neutral metal oxides with one or two electrons leads to formation of a three-center metal–metal bond [1]. The M–M distance and M–O–M angle decrease upon reduction as seen in Tables 1 and 2. The metal–metal interaction is stronger for the heavier systems with more diffuse d orbitals than for Cr. The electron localizability index (ELI), obtained by integrating the density in the basin of ELI-D at the molecular center, shows that for  $Cr_3O_9^-$  and  $Cr_3O_9^{2-}$  25% of the excess electrons are confined inside the metal-oxide ring. For the corresponding Mo and W compounds, roughly half of the excess charge is localized in the ELI-D basin inside the ring. The integrated ELI indices are given in Table 3. The density-difference plots reveal significant differences between the Cr compounds and the Mo and W oxides. For  $Cr_3O_9$ , the reduction increases the electron charge on the metals, on the oxygens, and also slightly at the ring center, whereas for  $Mo_3O_9$  and  $W_3O_9$  the excess electrons increase the electron density merely at the oxygens and in the ring center. The increase of electron density in the anionic  $Cr_3O_9$  species is not noticeable in the density-difference plots, whereas in the ELI-D plots the accumulation of electrons inside the ring can though be seen. The electron density at the Mo and W atoms is very little affected by reduction. Anionic and dianionic  $Cr_3O_9$  accumulates less electron density in the ring center than the Mo and W compounds, probably because the 3d orbitals of

Cr are more compact than the 4d and 5d orbitals of Mo and W. Electron density is also removed from the O–M–O bonds of the ring leading to longer O–M–O distances for the anions. The formation of the three-center metal–metal bond also affect the aromaticity properties and ring currents as discussed in Sect. 3.5.

### 3.3 Photoelectron spectra

The photodetachment energies (VDE and ADE) for simulating the photoelectron spectra (PES) of the  $Cr_3O_9^-$ ,  $Mo_3O_9^-$  and  $W_3O_9^-$  anions were calculated as described in Sect. 2. The corresponding singlet and triplet excitation energies, calculated at the B3LYP and CC2 levels, are given as supplementary material. The first VDEs and ADEs are listed in Table 4, where they are also compared with experimental and previously calculated values [3, 71, 1]. The first VDE, calculated at the DFT level, agrees well with previously reported theoretical and experimental values [3, 71, 1], whereas the VDE values calculated at the CC2 and MP2 levels for  $Mo_3O_9^-$  and  $W_3O_9^-$  of 1.98 eV/2.33 eV and 2.54 eV/2.94 eV are up to 2.0 eV smaller than the corresponding experimental results for  $Mo_3O_9^-$  and  $W_3O_9^-$  of 4.0 eV and 4.2 eV. Previous calculations at the coupled-cluster singles and doubles level with a perturbative triples correction (CCSD(T)) yielded VDEs for  $Mo_3O_9^-$  and  $W_3O_9^-$  of 3.92 eV and 3.85 eV, respectively, which are in good agreement with experiment [3, 71]. Thus, high-order correlation effects are important for the studied  $M_3O_9$  species, rendering the MP2 and CC2 calculations less reliable. For neutral  $Cr_3O_9$ , the ground-state calculation at the CC2 level did not converge. The lowest detachment energies for  $Mo_3O_9^-$  and  $W_3O_9^-$ , calculated at the HF SCF level, agree very well with experiment, whereas for  $Cr_3O_9^-$  the lowest VDE and ADE obtained at the HF SCF level are significantly larger than the experimental values, showing the importance of high-order electron correlation effects.

In the simulation of the PES of  $Mo_3O_9^-$  and  $W_3O_9^-$ , the first VDE calculated at the HF SCF level was taken as reference point. The obtained PES agree better with the experiment when the first VDE is calculated at the HF SCF level and the energies of the higher ionization channels are obtained by adding CC2 excitation energies to the first VDE. The lowest CC2 (HF SCF) and TD-DFT ionization energies of the calculated PES are given in Tables 5, 6, and 7, respectively, where the calculated values are also compared with experimental data.

The first VDE for  $Cr_3O_9^-$  calculated at the DFT level is about 0.2 eV larger than the experimental value. Experimentally, the second band of the PES appears at 6.22 eV and a broad band begins at 7 eV [3]. This feature is largely reproduced by the B3LYP calculations. The ionization

**Fig. 1** The density difference between the doubly charged anion and the neutral metal oxides are shown for **a**  $\text{Cr}_3\text{O}_9$ , **b**  $\text{Mo}_3\text{O}_9$ , and **c**  $\text{W}_3\text{O}_9$ . The electron localizability indicator (ELI) function is also shown for **d**  $\text{Mo}_3\text{O}_9^{2-}$ . The light areas correspond to increased electron density upon reduction. The corresponding plots for the other metal oxides are given as supplementary information. The density difference and the ELI graphs are visualized with OPENDX (<http://www.opendx.org/>) and gOpenMol [84, 85], respectively

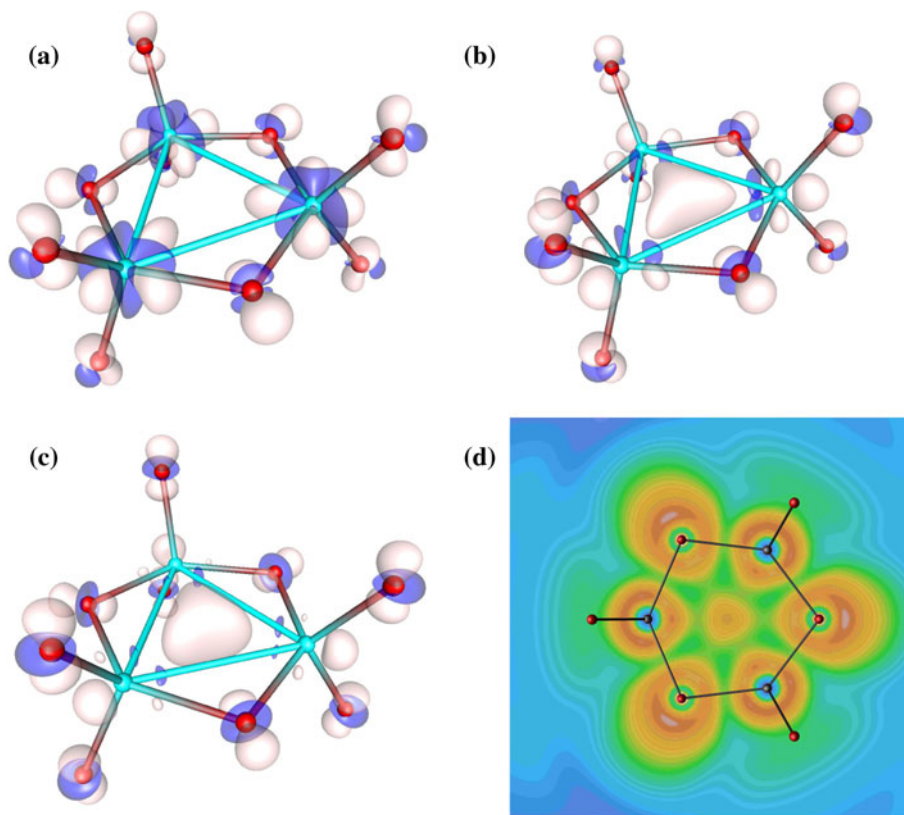


**Table 3** Integrated electron densities of the basin at the center of the ring defined by the electron localizability indicator

	Neutral	Anion	Dianion
$\text{Cr}_3\text{O}_9$	0.017	0.267	0.541
$\text{Mo}_3\text{O}_9$	0.216	0.738	1.105
$\text{W}_3\text{O}_9$	0.412	0.990	1.460
$\text{Sg}_3\text{O}_9$	0.513	1.142	1.694

The number of electrons are given for the neutral, the anion, and the dianion of the  $\text{Cr}_3\text{O}_9$ ,  $\text{Mo}_3\text{O}_9$ , and  $\text{W}_3\text{O}_9$  species

energy corresponding to the second band is 6.95 eV and above 7 eV we obtain many ionization channels. The ab initio methods completely fail to predict the PES of  $\text{Cr}_3\text{O}_9^-$ . For  $\text{Mo}_3\text{O}_9^-$  and  $\text{W}_3\text{O}_9^-$ , the CC2 calculations yield VDEs that are about 2 eV smaller than the experimental values. The first VDE of the metal-oxide anions calculated at the DFT level agree well with experimental data implying that the molecular structure can be identified by comparing calculated and experimental PES [1, 3, 4]. For

**Table 4** Calculated first vertical detachment energies (VDE in eV) and adiabatic detachment energies (ADE in eV) as compared with experimental data and to values obtained in other computational studies [1, 3, 71]

Molecule	DFT		CC2		CCSD(T)		MP2		HF SCF		Exp.	
	VDE	ADE	VDE	ADE	VDE	ADE	VDE	ADE	VDE	ADE	VDE	ADE
$\text{Cr}_3\text{O}_9^-$	4.97	4.59							16.14	15.27	4.75 <sup>a</sup>	4.44 <sup>a</sup>
Ref. [3]	5.18	4.85			4.54	4.23						
$\text{Mo}_3\text{O}_9^-$	3.84	3.23	1.98	1.94			2.33	1.81	4.49	3.43	4.0 <sup>b</sup>	3.5 <sup>b</sup>
Ref. [71]	4.16	3.43			3.92	3.29						
Ref. [1]	4.11	3.00										
$\text{W}_3\text{O}_9^-$	3.85	3.00	2.54	1.99			2.94	2.07	4.19	3.06	4.2 <sup>b</sup>	3.5 <sup>b</sup>
Ref. [71]	4.03	3.17			3.85	3.04						
Ref. [1]	4.39	3.00										

All calculations were carried out with the def2-TZVPP basis set

<sup>a</sup> Experimental values are taken from Ref. [3]

<sup>b</sup> Experimental values are taken from Ref. [1]

**Table 5** Vertical detachment energies (VDE in eV) of  $\text{Cr}_3\text{O}_9^-$  calculated at the B3LYP (DFT and TD-DFT) level are compared with experimental values [3]

VDE (B3LYP)	VDE (Exp.)
4.97	4.75 (X)
6.95 (T)	6.72 (A)
7.01 (T)	7.00 (Broad band)
7.03 (T)	
7.12 (T)	
7.20 (T)	

The spin of the final ionized state is denoted by T for triplet, respectively. The first singlet ionization channel lies at 7.36 eV

**Table 6** Vertical detachment energies (VDE in eV) of  $\text{Mo}_3\text{O}_9^-$  calculated at the B3LYP (DFT and TD-DFT) and CC2 levels are compared with experimental values [1]

VDE (B3LYP)	VDE (CC2)	VDE (Exp.)
3.84	4.49	4.0
6.81 (T)	6.15 (S)	7.6 (Broad band)
6.82 (T)	6.18 (T)	
6.84 (T)	6.72 (S)	
7.01 (S)	6.72 (T)	
7.02 (S)	6.73 (S)	

The spin of the final ionized state is denoted by S and T for singlet and triplet, respectively

**Table 7** Vertical detachment energies (VDE in eV) of  $\text{W}_3\text{O}_9^-$  calculated at the B3LYP (DFT and TD-DFT) and CC2 levels are compared with experimental values [1]

VDE (B3LYP)	VDE (CC2)	VDE (Exp.)
3.85	4.19	4.2
6.73 (T)	5.96 (S)	7.0 (Broad band starting)
6.74 (T)	5.98 (T)	
6.83 (S)	6.79 (T)	
6.83 (S)	6.80 (T)	
6.95 (T)	6.81 (S)	
7.12 (S)	7.34 (S)	

The spin of the final ionized state is denoted by S and T for singlet and triplet, respectively

$\text{Mo}_3\text{O}_9^-$ , the ionization energies of the higher transitions are underestimated at both the B3LYP and the CC2 levels, whereas for  $\text{W}_3\text{O}_9^-$  the B3LYP ionization energies agree within 0.3 eV with experimental results.

### 3.4 Aromatic ring-current shieldings

An approximate relation between the nuclear magnetic shielding  $\sigma(z)$  along the molecular symmetry axis and the

size of the ring current susceptibility  $\left(\frac{\partial I}{\partial B_{\text{ex}}}\right)$  is obtained when assuming that the wire carrying the ring current is circular and infinitely thin and that the current is flowing in the molecular plane. The obtained aromatic ring-current shieldings (ARCS) relation between the shieldings and the current susceptibility is [42]

$$\sigma(z) = -\frac{\mu_0}{2} \left( \frac{\partial I}{\partial B_{\text{ex}}} \right) \frac{R^2}{(z^2 + R^2)^{\frac{3}{2}}} \quad (1)$$

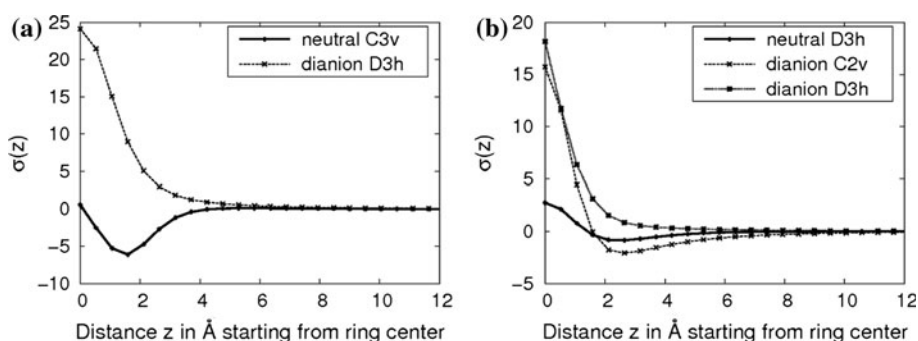
where  $\mu_0$  is the vacuum permeability,  $R$  the current loop radius and  $z$  the perpendicular distance from the loop center. The shape of the shielding function  $\sigma(z)$  indicates whether the molecule is aromatic, antiaromatic, or nonaromatic, whereas fitting the calculated shieldings to Eq. (1) yields an estimate for the ring-current strength corresponding to the degree of aromaticity [42, 73]. The shielding function at  $z = 0$  and  $z = 1$  Å can directly be related to the nucleus-independent chemical shift values NICS(0) and NICS(1) [74]. The calculated shielding functions  $\sigma(z)$  for  $\text{Cr}_3\text{O}_9$ ,  $\text{Cr}_3\text{O}_9^{2-}$  and  $\text{Mo}_3\text{O}_9$ ,  $\text{Mo}_3\text{O}_9^{2-}$  are depicted in Fig. 2. The shielding functions of  $\text{Cr}_3\text{O}_9^{2-}$  and  $\text{Mo}_3\text{O}_9^{2-}$  with  $D_{3h}$  symmetry show the typical curve shape of an aromatic molecule, whereas judged from the shape of the ARCS curve, a nonaromatic character can be assumed for the neutral  $\text{Cr}_3\text{O}_9$  and  $\text{Mo}_3\text{O}_9$  molecules. For  $\text{Mo}_3\text{O}_9^{2-}$  of  $C_{2v}$  symmetry, the ARCS calculation indicates presence of paratropic and diatropic currents, but suggests an overall nonaromatic character of the molecule. The negative long-ranged magnetic shielding function indicates that the molecules cannot sustain a strong diatropic ring current. On the other hand, using exclusively the NICS(0) and NICS(1) values to assess the aromaticity leads to the following assignment of the aromatic character of the chromium and molybdenum oxides:  $\text{Cr}_3\text{O}_9$  (nonaromatic),  $\text{Mo}_3\text{O}_9$  (weakly aromatic),  $\text{Cr}_3\text{O}_9^{2-}$ , and  $\text{Mo}_3\text{O}_9^{2-}$  (strongly aromatic). The aromatic characters obtained by the ARCS and NICS approaches are not concordant. For  $\text{Mo}_3\text{O}_9^{2-}$  ( $C_{2v}$ ), the large magnetic shielding in the ring center seems to originate from the excess electron density forming three-center metal–metal bonds, because the molecular ring does not sustain any strong ring current as discussed in Sect. 3.2.

### 3.5 Magnetically induced current densities

The calculated magnetically induced current densities and current-strength functions of  $\text{Cr}_3\text{O}_9^{0/2-}$  and  $\text{Mo}_3\text{O}_9^{0/2-}$  are depicted in Figs. 3 and 4. The current-strength function with respect to the distance  $x$  starting at the ring center and passing a selected bond has been calculated. For a planar molecule such as benzene, the integration plane can be placed perpendicularly to the molecular ring passing the bond of interest with an angle of 90°. Here, the geometries



**Fig. 2** The calculated ARCS shielding functions for **a**  $\text{Cr}_3\text{O}_9$  ( $C_{3v}$ , not aromatic) and  $\text{Cr}_3\text{O}_9^{2-}$  ( $D_{3h}$ , aromatic), **b**  $\text{Mo}_3\text{O}_9$  ( $D_{3h}$ , not aromatic),  $\text{Mo}_3\text{O}_9^{2-}$  ( $C_{2v}$ , weakly aromatic), and  $\text{Mo}_3\text{O}_9^{2-}$  ( $D_{3h}$ , aromatic). The graphs have been made with GNUPLOT (<http://www.gnuplot.info>)



of the investigated molecules make it impossible to place the integration plane such that it simultaneously passes the ring center, lies exactly perpendicularly to the molecular ring plane, and crosses the middle of the O–M–O bond with an angle of  $90^\circ$ . Furthermore, some of the investigated transition-metal oxides are nonplanar. The current strength function has been evaluated by placing the integration plane such that it goes through the ring center and passes the middle of the O–M–O bond and lies perpendicularly to the molecular plane. The integration plane is not perpendicular to the O–M–O bond of the ring, but forms an angle of  $60^\circ$  with respect to the bond.

### 3.5.1 $\text{Cr}_3\text{O}_9$

The current density of  $\text{Cr}_3\text{O}_9$  ( $C_{3v}$ ) is visualized in Fig. 3a. Neither a diatropic nor a paratropic current path circling around the whole molecular ring is observed, indicating that the system is nonaromatic. The current-strength function of  $\text{Cr}_3\text{O}_9$  is depicted in Fig. 4a. It shows that inside the molecular ring, a paratropic current circles until the Cr–O bond is passed. At  $x = 1.5$  Å *i.e.*, at the O–M–O bond, a small shoulder is seen, whereas the main diatropic current contribution appears outside the ring. At larger  $x$  values, the diatropic current dominates. The amount of diatropic and paratropic currents almost cancel, resulting in a total ring-current strength of  $-1.1$  nA/T.  $\text{Cr}_3\text{O}_9$  is very weakly antiaromatic or nonaromatic according to the ring-current criterion, as also obtained from the ARCS plots. The NICS(0) and NICS(1) calculations suggest that  $\text{Cr}_3\text{O}_9$  is nonaromatic and weakly antiaromatic, respectively.

### 3.5.2 $\text{Cr}_3\text{O}_9^{2-}$

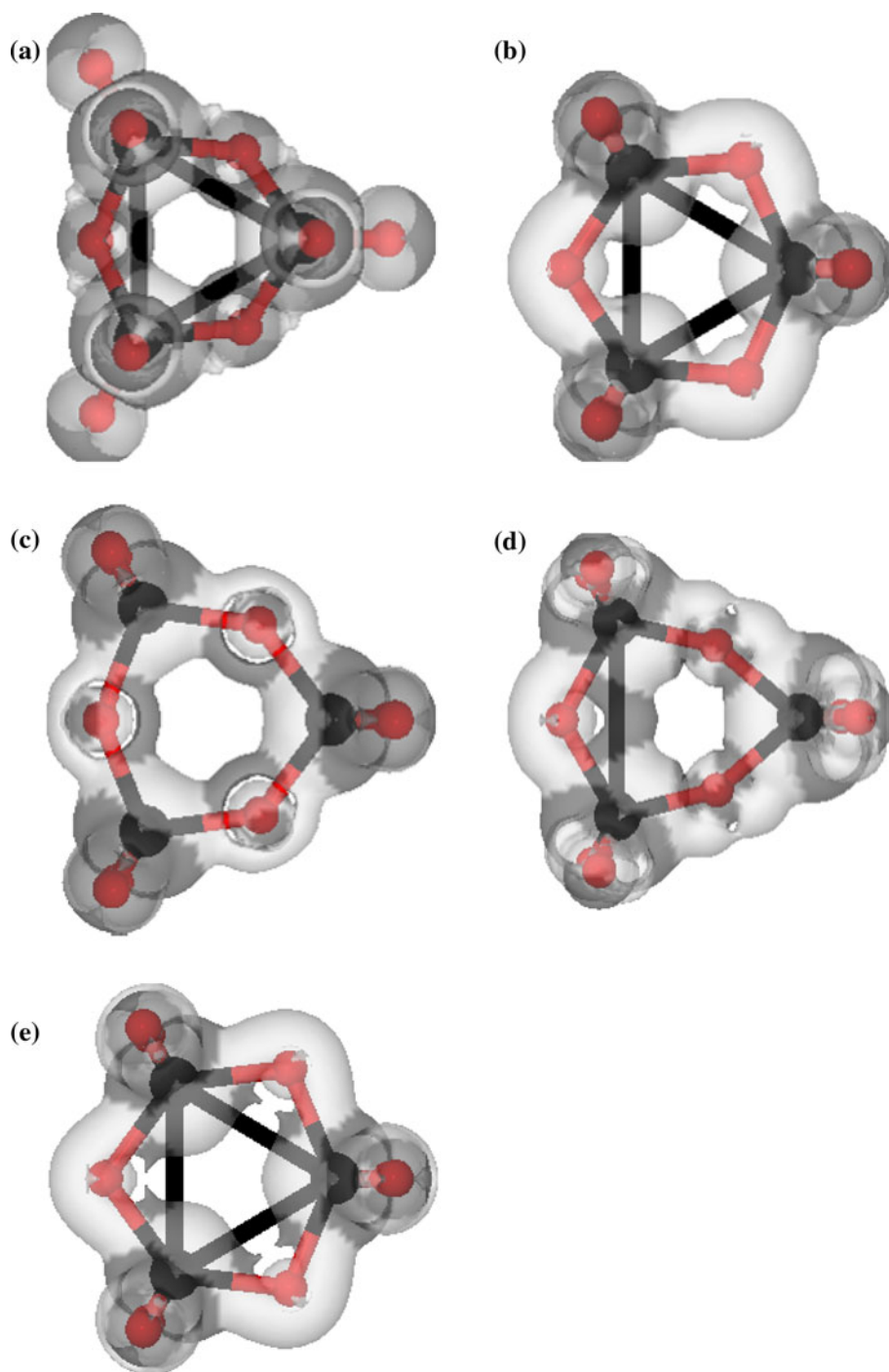
The current density of the  $\text{Cr}_3\text{O}_9^{2-}$  anion ( $D_{3h}$ ) is visualized in Fig. 3b. A diatropic current flowing around the whole molecular ring is clearly seen, suggesting that the molecule is aromatic. The current is split at the  $\text{CrO}_2$  moieties into a diatropic part taking the route along the inner side of the ring and into a paratropic one circling around the two  $\text{CrO}_2$

oxygens. The current-strength function of  $\text{Cr}_3\text{O}_9^{2-}$  is depicted in Fig. 4b. A strong diatropic current circles inside and outside the molecular ring dominating the whole system. In the current-strength profile, no paratropic current is seen. This is confirmed by investigating the diatropic and paratropic contributions to the total net current strength in detail as depicted in Fig. 5a. The graph in Fig. 5a shows that the paratropic contribution to the total ring-current strength is almost zero. The Cr–O bond is passed at  $x = 1.55$  Å. The first maximum in the curve is therefore assigned to current transport in 3d orbitals directed along the O–M–O bonds. The compact 3d orbitals of Cr are not able to form a significant three-center two-electron metal–metal bond that could transport the ring current. The small shoulder on the inside of the main peak might though originate from a weak metal–metal interaction. The outer peak in the current profile reminds of the diatropic current contribution obtained for neutral  $\text{Cr}_3\text{O}_9$ . The total ring-current strength of  $17.2$  nA/T is larger than the one of  $11.8$  nA/T for benzene. Thus,  $\text{Cr}_3\text{O}_9^{2-}$  is aromatic according to the ring-current criterion, as also deduced from the ARCS plots. The NICS calculations also suggest that  $\text{Cr}_3\text{O}_9^{2-}$  is aromatic.

### 3.5.3 $\text{Mo}_3\text{O}_9$

The current density of  $\text{Mo}_3\text{O}_9$  ( $D_{3h}$ ) is visualized in Fig. 3c. A weak diatropic current path flowing around the whole molecular ring is observed. Compared with the current path seen for  $\text{Cr}_3\text{O}_9^{2-}$ , the one for  $\text{Mo}_3\text{O}_9$  appears to be more complicated, because the current flow is split twice. As for  $\text{Cr}_3\text{O}_9^{2-}$ , the current is split at the  $\text{MoO}_2$  moieties into a paratropic part circling at the  $\text{MoO}_2$  oxygens and a diatropic part taking the inner route along the molecular ring. When passing the ring oxygens, a second current split appears. The current is split into a diatropic part, which takes the route outside the ring oxygens and into a paratropic one passing inside the molecular ring. The current-path structure obtained for the neutral  $\text{Mo}_3\text{O}_9$  oxide does not allow a clear assignment of the aromatic nature of the

**Fig. 3** The magnetically induced current density calculated for **a**  $\text{Cr}_3\text{O}_9$  ( $C_{3v}$ ), **b**  $\text{Cr}_3\text{O}_9^{2-}$  ( $D_{3h}$ ), **c**  $\text{Mo}_3\text{O}_9$  ( $D_{3h}$ ), **d**  $\text{Mo}_3\text{O}_9^{2-}$  ( $C_{2v}$ ) and **e**  $\text{Mo}_3\text{O}_9^{2-}$  ( $D_{3h}$ ). Diatropic currents are light grey and the paratropic ones are darker. The pictures have been made with JMOL (<http://www.jmol.org>)



molecule, but indicates local circulation of the current rather than presence of a global ring current.

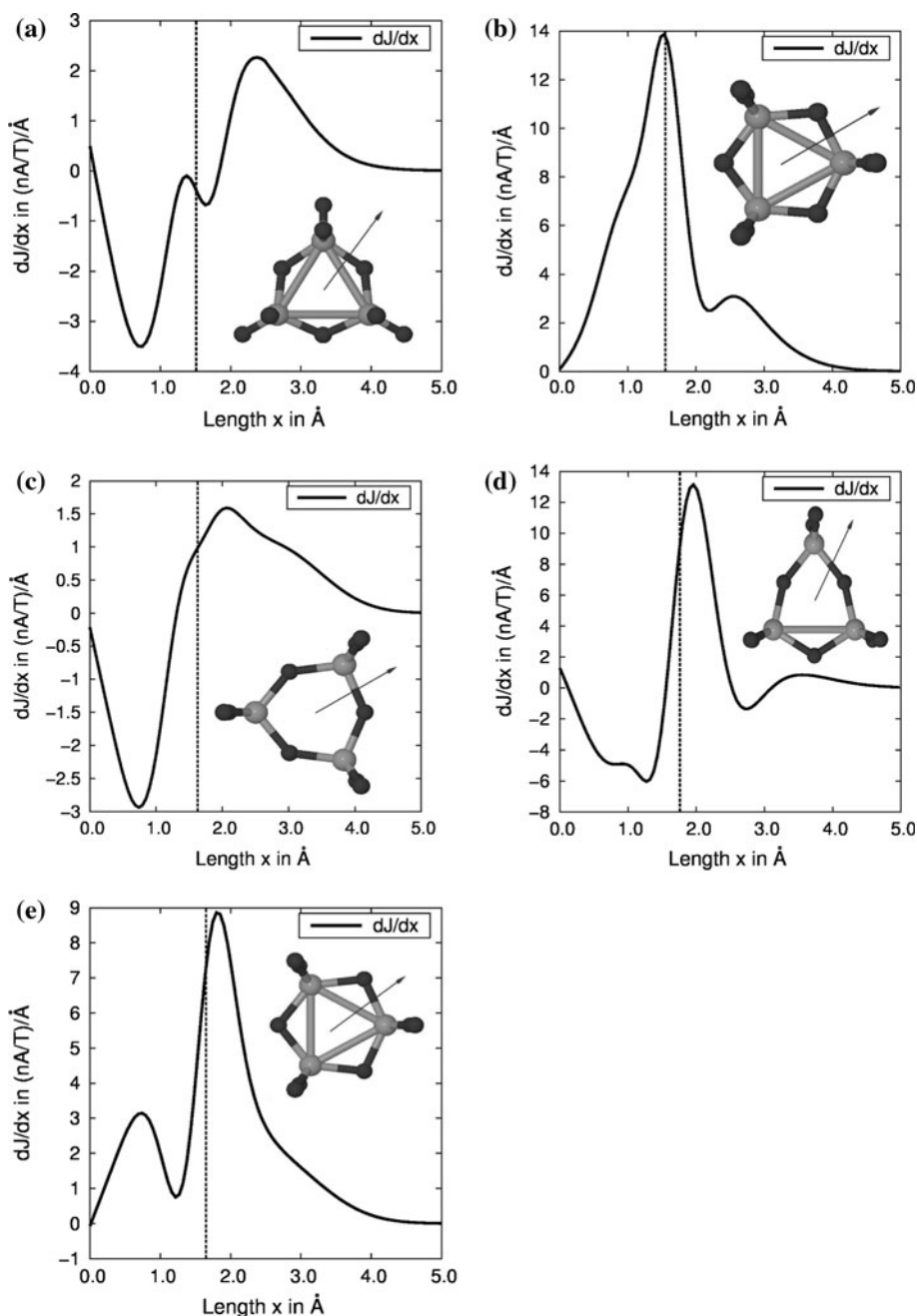
The current-strength profile of  $\text{Mo}_3\text{O}_9$  is depicted in Fig. 4c. It shows that a paratropic current flows inside the Mo–O bond, whereas after  $x = 1.0 \text{ \AA}$  and outside the bond at  $x = 1.63 \text{ \AA}$ , the diatropic current dominates. The diatropic and paratropic current contributions almost cancel, resulting in a total ring-current strength of  $0.3 \text{ nA/T}$ .  $\text{Mo}_3\text{O}_9$  is nonaromatic according to the ring-current

criterion, as also obtained from the ARCS plots. The NICS values suggest a weakly aromatic or an almost nonaromatic  $\text{Mo}_3\text{O}_9$  ring.

#### 3.5.4 $\text{Mo}_3\text{O}_9^{2-}$

The current density of  $\text{Mo}_3\text{O}_9^{2-}$ , calculated in  $C_{2v}$  symmetry, is depicted in Fig. 3d. It shows that a noninterrupted diamagnetic current flows around the whole molecular

**Fig. 4** The current-strength functions calculated for **a**  $\text{Cr}_3\text{O}_9$  ( $C_{3v}$ ), **b**  $\text{Cr}_3\text{O}_9^{2-}$  ( $D_{3h}$ ), **c**  $\text{Mo}_3\text{O}_9$  ( $D_{3h}$ ), **d**  $\text{Mo}_3\text{O}_9^{2-}$  ( $C_{2v}$ ) and **e**  $\text{Mo}_3\text{O}_9^{2-}$  ( $D_{3h}$ ) with respect to the distance  $x$  along the arrow in the graphs. The orientation of the integration plane perpendicular to the molecular ring is indicated by the arrow. The current strength profile starts at the center of the ring and goes through the O–M–O bond. The O–M–O bond is passed at **a** 1.51 Å, **b** 1.55 Å, **c** 1.63 Å, **d** 1.76 Å and **e** 1.65 Å. The total ring-current strengths are **a**  $-1.1$  nA/T, **b**  $17.2$  nA/T, **c**  $0.3$  nA/T, **d**  $1.9$  nA/T and **e**  $10.9$  nA/T. The graphs have been made with GNUPLOT (<http://www.gnuplot.info>) and JMOL (<http://www.jmol.org>)



ring. In contrast to neutral  $\text{Mo}_3\text{O}_9$ , the current splits at the Mo centers into a paratropic one circling around the Mo center. A diatropic current circles around the  $\text{MoO}_2$  oxygens disrupting a smooth diatropic or paratropic current flow around the whole molecule. The current path splits at the ring oxygens as for the neutral molecule.

The current-strength profile of  $\text{Mo}_3\text{O}_9^{2-}$  ( $C_{2v}$ ) is depicted in Fig. 4d. A strong paratropic current circles inside the molecular ring. The Mo–O bond is passed at  $x = 1.76$  Å, where also a narrow maximum is seen in the curve. Diatropic currents mainly dominate outside the molecular ring with small alternating paratropic and diatropic

contributions farther out, yielding a weak net ring-current strength of  $1.9$  nA/T.  $\text{Mo}_3\text{O}_9^{2-}$  ( $C_{2v}$ ) is very weakly aromatic or even nonaromatic, which agrees with the results obtained from the ARCS plots. The NICS calculations suggests that it is aromatic. The reason for the failure of the NICS prediction of the degree of aromaticity for  $\text{Mo}_3\text{O}_9^{2-}$  is the presence of the electron density in the ring center shielding the external magnetic field.

The current density of  $\text{Mo}_3\text{O}_9^{2-}$ , calculated in  $D_{3h}$  symmetry, is depicted in Fig. 3e. A strong diatropic current flowing around the molecular ring is clearly seen. The current-strength profile of  $\text{Mo}_3\text{O}_9^{2-}$  ( $D_{3h}$ ) in Fig. 4e shows

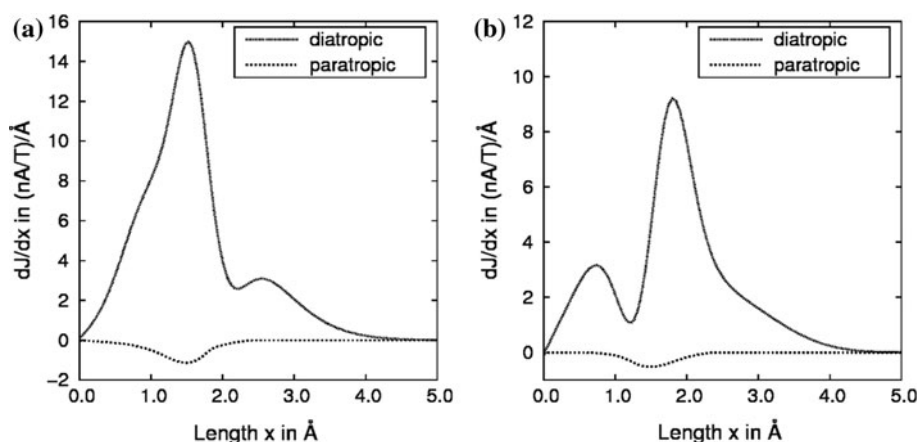


**Fig. 5** The calculated diatropic and paratropic contributions to the total current-strength functions for **a** Cr<sub>3</sub>O<sub>9</sub><sup>2-</sup> (*D*<sub>3h</sub>) and **b** Mo<sub>3</sub>O<sub>9</sub><sup>2-</sup> (*D*<sub>3h</sub>) with respect to the distance *x*. The orientation of the integration plane perpendicular to the molecular ring is the same as in Fig. 4. The

current-strength profile starts at the center of the ring and goes through the O–M–O bond, *M* = Cr, Mo. The O–M–O bond is passed at **a** 1.55 Å, and **b** at 1.65 Å. The graphs have been made with GNUPLOT (<http://www.gnuplot.info>)

that strong diatropic currents circle inside and outside the molecular ring. As for Cr<sub>3</sub>O<sub>9</sub><sup>2-</sup>, no paratropic currents are seen. This is confirmed by a detailed study of the diatropic and paratropic contributions to the total net current strength shown in Fig. 5b. The graph shows that the paratropic contribution to the total ring-current strength is almost zero. The Mo–O bond is passed at *x* = 1.65 Å, thus the first maximum in the curve originates from currents sustained by the excess electrons in the three-center two-electron metal–metal bond. The total ring-current strength of 10.9 nA/T is as strong as the one for benzene. Mo<sub>3</sub>O<sub>9</sub><sup>2-</sup> (*D*<sub>3h</sub>) is aromatic according to the ring-current criterion, as also obtained from the ARCS plots and the NICS calculations.

#### 4 Summary and conclusions

The molecular structures of the group 6 transition-metal oxides were optimized using a variety of density functionals (see the electronic supplementary material). The obtained molecular structures largely agree, even though the metal oxides are found to be very floppy. For W<sub>3</sub>O<sub>9</sub><sup>-</sup>, the BP86 calculations yield a *D*<sub>3h</sub> structure, whereas at the TPSS level, the anion has a Jahn-Teller distorted *C*<sub>2v</sub> structure. Structure optimization of Cr<sub>3</sub>O<sub>9</sub><sup>-</sup> and Mo<sub>3</sub>O<sub>9</sub><sup>-</sup> at the TPSS level also yielded Jahn-Teller distorted molecules. Mo<sub>3</sub>O<sub>9</sub><sup>2-</sup> has two low-lying structures. The energetically lowest structure has *D*<sub>3h</sub> symmetry. A structure of *C*<sub>2v</sub> symmetry lies 93 kJ/mol higher in energy. The symmetry of the molecular structure of the lowest metal oxides obtained using the TPSS functional are: Cr<sub>3</sub>O<sub>9</sub> (*C*<sub>3v</sub>), Cr<sub>3</sub>O<sub>9</sub> (*C*<sub>s</sub>), Cr<sub>3</sub>O<sub>9</sub><sup>2-</sup> (*D*<sub>3h</sub>), Mo<sub>3</sub>O<sub>9</sub> (*D*<sub>3h</sub>), Mo<sub>3</sub>O<sub>9</sub><sup>-</sup> (*C*<sub>2v</sub>), Mo<sub>3</sub>O<sub>9</sub><sup>2-</sup> (*D*<sub>3h</sub>), W<sub>3</sub>O<sub>9</sub> (*D*<sub>3h</sub>), W<sub>3</sub>O<sub>9</sub><sup>-</sup> (*C*<sub>2v</sub>), W<sub>3</sub>O<sub>9</sub><sup>-</sup> (*D*<sub>3h</sub> using BP86), W<sub>3</sub>O<sub>9</sub><sup>2-</sup> (*D*<sub>3h</sub>), Sg<sub>3</sub>O<sub>9</sub> (*D*<sub>3h</sub> using BP86),

Sg<sub>3</sub>O<sub>9</sub><sup>-</sup> (*D*<sub>3h</sub> using BP86), and Sg<sub>3</sub>O<sub>9</sub><sup>2-</sup> (*D*<sub>3h</sub> using BP86). The BP86 functional used in the ADF optimization of the tungsten and seaborgium compounds did not yield any Jahn-Teller distorted structure for the singly charged W<sub>3</sub>O<sub>9</sub><sup>-</sup> anion.

Photodetachment energies of M<sub>3</sub>O<sub>9</sub><sup>-</sup> (*M* = Cr, Mo, W) have been calculated at the DFT and CC2 levels for simulation of their PES. The VDEs calculated at the DFT level agree well with experimental values and with values obtained in previous computational studies, whereas the PES calculated at the CC2 level are not very accurate. High-order correlation effects appear to be important at ab initio levels. For Cr<sub>3</sub>O<sub>9</sub><sup>-</sup>, the CC2 ground-state calculation did not converge, suggesting that the wave function has a significant multi-reference character.

Magnetically induced current densities and current strengths have been investigated for the neutral and dianionic Cr<sub>3</sub>O<sub>9</sub> and Mo<sub>3</sub>O<sub>9</sub> species to assign their aromatic character. The degree of aromaticity was obtained with explicit calculations of the ring-current strengths using the GIMIC method. The obtained aromatic properties are largely consistent with those deduced from the ARCS calculations. NICS calculations on neutral Mo<sub>3</sub>O<sub>9</sub> indicate that it can be considered to be weakly aromatic, whereas the GIMIC calculation shows that the molecular ring sustains a very weak ring current of 0.3 nA/T. NICS calculations suggest that Mo<sub>3</sub>O<sub>9</sub><sup>2-</sup> (*C*<sub>2v</sub>) is strongly aromatic, whereas GIMIC calculations yield a net ring-current strength of 1.9 nA/T, which is only 16% of the ring-current strength for benzene. Mo<sub>3</sub>O<sub>9</sub><sup>2-</sup> (*C*<sub>2v</sub>) is thus very weakly aromatic or almost nonaromatic. Mo<sub>3</sub>O<sub>9</sub><sup>2-</sup> (*D*<sub>3h</sub>) is on the other hand found to be aromatic with a ring-current strength of 10.9 nA/T. The study shows that the Mo<sub>3</sub>O<sub>9</sub><sup>2-</sup> structure of *C*<sub>2v</sub> symmetry does not sustain a noninterrupted diatropic current path



flowing around the whole molecular ring. Instead, the current density seems to consist of local vortices. For  $\text{Mo}_3\text{O}_9^{2-}$  ( $D_{3h}$ ), a strong diatropic ring current flows around the molecular ring. The study shows that integration of the magnetically induced current density is necessary for obtaining reliable information about the aromatic character of the transition-metal oxides. NICS calculations are found to lead to an incorrect assignment of the molecular aromaticity of the  $\text{Mo}_3\text{O}_9$  species. The long-ranged magnetic shielding function used in the ARCS method reveals problems with NICS calculations. GIMIC calculations are needed for a reliable assignment of the aromaticity.

Geometrical changes are known to play an important role when investigating the aromatic character of a molecule. Metal–metal distances are shorter for the negatively charged species rendering a higher electron delocalization and a larger current flow around the molecular ring possible. Planar molecules and short metal–metal distances are though not enough to make the studied species aromatic, as shown by calculations on neutral  $\text{Cr}_3\text{O}_9$  and  $\text{Mo}_3\text{O}_9$ . Addition of two electrons makes  $\text{Cr}_3\text{O}_9^{2-}$  ( $D_{3h}$ ) and  $\text{Mo}_3\text{O}_9^{2-}$  ( $D_{3h}$ ) aromatic, which can be understood by counting the number of electrons. The metal centers of the neutral molecules are hexavalent implying that the  $d$ -orbitals are formally empty. The two free-electron pairs of the ring oxygens have four  $\pi$ -electrons. Thus, when adding two electrons, the Hückel  $4n + 2$  rule for aromaticity is fulfilled for the doubly charged anions, providing a simple explanation for their aromatic character. However, the weak aromaticity of  $\text{Mo}_3\text{O}_9^{2-}$  ( $C_{2v}$ ) cannot be explained by this simple rule of thumb.

In aromatic hydrocarbons, the current flowing on the inside of the molecular ring is paratropic and the current outside it is diatropic. The strength of the diatropic current is larger than the paratropic one leading to a net diatropic current. The current profiles of the investigated dianionic aromatic transition-metal oxides show that they have no paratropic contributions to the ring current. In Fig. 5b, a double peak structure is seen in the ring-current profile of  $\text{Mo}_3\text{O}_9^{2-}$  ( $D_{3h}$ ). The first peak indicates that a current flows between the metal atoms, probably sustained by the  $d$ -orbitals, giving evidence for  $d$ -orbital aromaticity. The outer peak represents ring-current flow via the ring oxygens. Comparison of the two graphs in Fig. 5 indicates that  $\text{Mo}_3\text{O}_9^{2-}$  ( $D_{3h}$ ) has a much stronger ring current inside the metal-oxide ring than  $\text{Cr}_3\text{O}_9^{2-}$  ( $D_{3h}$ ), even though the Cr compound has a larger net ring-current strength.

The total ring-current strengths for  $\text{Cr}_3\text{O}_9$  ( $C_{3v}$ ),  $\text{Cr}_3\text{O}_9^{2-}$  ( $D_{3h}$ ),  $\text{Mo}_3\text{O}_9$  ( $D_{3h}$ ),  $\text{Mo}_3\text{O}_9^{2-}$  ( $C_{2v}$ ), and  $\text{Mo}_3\text{O}_9^{2-}$  ( $D_{3h}$ ) are  $-1.1$  nA/T,  $17.2$  nA/T,  $0.3$  nA/T,  $1.9$  nA/T, and  $10.9$  nA/T, respectively, suggesting that only  $\text{Cr}_3\text{O}_9^{2-}$  ( $D_{3h}$ ) and  $\text{Mo}_3\text{O}_9^{2-}$  ( $D_{3h}$ ) are aromatic, which is also supported by the ARCS calculations. The NICS calculations incorrectly

propose that also  $\text{Mo}_3\text{O}_9^{2-}$  ( $C_{2v}$ ) sustains a significant ring current in the presence of an external magnetic field.

**Acknowledgments** This research has been supported by the Academy of Finland through its Centers of Excellence Programme 2006–2011 and by Postdoctoral Researcher's project (126905). H. F. was funded from the Research Grant Motions in Macromolecular Function: New Approaches to Visualize and Simulate Protein Flexibility, awarded 2008 by the Human Frontier of Science Program (HFSP). We thank CSC – the Finnish IT Center for Science for computer time. This article is dedicated to Prof. Pekka Pyykkö on his 70th birthday. The research interests of Prof. Pyykkö comprise relativistic effects and computational inorganic chemistry. He has published nine articles on studies of Cr, Mo, and W compounds showing his interest in the chromium, molybdenum, and tungsten chemistry [75–83].

## References

- Huang X, Zhai HJ, Kiran B, Wang LS (2005) Angew Chem Int Ed 44:7251. doi:10.1002/anie.200502678
- Huang X, Zhai HJ, Li J, Wang LS (2006) J Phys Chem A 110:85
- Zhai HJ, Li S, Dixon DA, Wang LS (2008) J Am Chem Soc 130:5167
- Huang X, Zhai HJ, Waters T, Li J, Wang LS (2006) Angew Chem Int Ed 45:657
- Zhai HJ, Averkiev BB, Zubarev DY, Wang LS, Boldyrev AI (2007) Angew Chem Int Ed 46:4277. doi:10.1002/anie.200700442
- Rothgeb DW, Hossain E, Kuo AT, Troyer JL, Jarrold CC (2009) J Chem Phys 131:044310. doi:10.1063/1.3180825
- Mayhall NJ, Rothgeb DW, Hossain E, Raghavachari K, Jarrold CC (2009) J Chem Phys 130:124313. doi:10.1063/1.3100782
- Li S, Zhai HJ, Wang LS, Dixon DA (2009) J Phys Chem A 113:11273. doi:10.1021/jp9082008
- Zhai HJ, Wang B, Huang X, Wang LS (2009) J Phys Chem A 113:9804. doi:10.1021/jp905478w
- Zhai HJ, Wang B, Huang X, Wang LS (2009) J Phys Chem A 113:3866. doi:10.1021/jp809945n
- Chen WJ, Zhai HJ, Zhang YF, Huang X, Wang LS (2010) J Phys Chem A 114:5958. doi:10.1021/jp102439v
- Averkiev BB, Boldyrev AI (2007) J Phys Chem Lett 111:12864. doi:10.1021/jp077528b
- Wang B, Chen WJ, Zhao BC, Zhang YF, Huang X (2010) J Phys Chem A 114:1964. doi:10.1021/jp909676s
- Mayhall NJ, Becher EL III, Chowdhury A, Raghavachari K (2011) J Phys Chem A 115:2291. doi:10.1021/jp108344k
- Foroutan-Nejad C, Shahbazian S, Parviz-Ranjbar P (2011) Phys Chem Chem Phys 13:4576. doi:10.1039/C0CP01519A
- Gong Y, Zhou M (2009) Chem Rev 109:6765. doi:10.1021/cr900185x
- Böhme DK, Schwarz H (2005) Angew Chem Int Ed 44:2336
- King RB (1991) Inorg Chem 30:4437. doi:10.1021/ic00023a030
- Wannere CS, Corminboeuf C, Wang ZX, Wodrich MD, King RB, von Ragué Schleyer P (2005) J Am Chem Soc 127:5701
- Lin YC, Sundholm D, Jusélius J, Cui LF, Li X, Zhai HJ, Wang LS (2006) J Phys Chem A 110:4244
- Li X, Kuznetsov AE, Zhang HF, Boldyrev AI, Wang LS (2001) Science 291:859
- Kuznetsov AE, Boldyrev AI, Li X, Wang LS (2001) J Am Chem Soc 123:8825
- Kuznetsov AE, Birch KA, Boldyrev AI, Li X, Zhai HJ, Wang LS (2003) Science 300:622



24. Chen Z, Corminboeuf C, Heine T, Bohmann J, von Ragué Schleyer P (2003) *J Am Chem Soc* 125:13930
25. Havenith RWA, Fowler PW, Steiner E, Shetty S, Kanhere D, Pal S (2004) *Phys Chem Chem Phys* 6:285
26. Ritter SK (2003) *Chem Eng News* 81(50):23
27. Lin YC, Jusélius J, Sundholm D, Gauss J (2005) *J Chem Phys* 122:214308
28. Jusélius J, Sundholm D, Gauss J (2004) *J Chem Phys* 121:3952
29. Fliegl H, Sundholm D, Taubert S, Jusélius J, Klopper W (2009) *J Phys Chem A* 113:8668. doi:[10.1021/jp9029776](https://doi.org/10.1021/jp9029776)
30. Islas R, Heine T, Merino G (2007) *J Chem Theory Comput* 3:775
31. Johansson MP, Jusélius J, Sundholm D (2005) *Angew Chem Int Ed* 44:1843
32. Johansson MP, Jusélius J (2005) *Lett Org Chem* 2:469
33. Lin YC, Sundholm D, Jusélius J (2006) *J Chem Theory Comput* 2:761
34. Jusélius J, Sundholm D (2008) *Phys Chem Chem Phys* 10:6630
35. Taubert S, Jusélius J, Sundholm D, Klopper W, Fliegl H (2008) *J Phys Chem A* 112:13584
36. Taubert S, Sundholm D, Pichierri F (2009) *J Org Chem* 74:6495
37. Taubert S, Sundholm D, Pichierri F (2010) *J Org Chem* 75:5867. doi:[10.1021/jo100902w](https://doi.org/10.1021/jo100902w)
38. Taubert S, Kaila VRI, Sundholm D (2011) *Int J Quant Chem* 111:848. doi:[10.1002/qua.22869](https://doi.org/10.1002/qua.22869)
39. Fliegl H, Sundholm D, Taubert S, Pichierri F (2010) *J Phys Chem A* 114:7153. doi:[10.1021/jp1021517](https://doi.org/10.1021/jp1021517)
40. Fliegl H, Lehtonen O, Sundholm D, Kaila VRI (2010) *Phys Chem Chem Phys* 13:434. doi:[10.1039/C0CP00622J](https://doi.org/10.1039/C0CP00622J)
41. von Ragué Schleyer P, Maerker C, Dransfeld A, Jiao H, van Eikema Hommes NJR (1996) *J Am Chem Soc* 118:6317
42. Jusélius J, Sundholm D (1999) *Phys Chem Chem Phys* 1:3429
43. Morao I, Cossío FP (1999) *J Org Chem* 64:1868. doi:[10.1021/jo981862+](https://doi.org/10.1021/jo981862+)
44. Ahlrichs R, Bär M, Häser M, Horn H, Kölmel C (1989) *Chem Phys Lett* 162:165. Current version: see <http://www.turbomole.com>
45. Tao J, Perdew JP, Staroverov VN, Scuseria GE (2003) *Phys Rev Lett* 91:1464011
46. Weigend F, Ahlrichs R (2005) *Phys Chem Chem Phys* 7:3297
47. Furche F, Perdew JP (2006) *J Chem Phys* 124:044103. doi:[10.1063/1.2162161](https://doi.org/10.1063/1.2162161)
48. Andrae D, Häussermann U, Dolg M, Stoll H, Preuss H (1990) *Theor Chim Acta* 77:123
49. Perdew JP, Burke K, Ernzerhof M (1996) *Phys Rev Lett* 77:3865
50. te Velde G, Bickelhaupt FM, van Gisbergen SJA, Fonseca Guerra C, Baerends EJ, Snijders JG, Ziegler T (2001) *J Comp Chem* 22:931
51. Fonseca Guerra C, Snijders JG, te Velde G, Baerends EJ (1998) *Theor Chem Acc* 99:391
52. Baerends EJ, Ziegler T, Autschbach J, Bashford D, Bérces A, Bickelhaupt FM, Bo C, Boerrigter PM, Cavallo L, Chong DP, Deng L, Dickson RM, Ellis DE, van Faassen M, Fan L, Fischer TH, Fonseca Guerra C, Ghysels A, Giammona A, van Gisbergen SJA, Götz AW, Groeneveld JA, Gritsenko OV, Grüning M, Gusarov S, Harris FE, van den Hoek P, Jacob CR, Jacobsen H, Jensen L, Kaminski JW, van Kessel G, Kootstra F, Kovalenko A, Krykunov MV, van Lenthe E, McCormack DA, Michalak A, Mitoraj M, Neugebauer J, Nicu VP, Noodleman L, Osinga VP, Patchkovskii S, Philipsen PHT, Pye DPCC, Ravenek W, Rodríguez JJ, Ros P, Schipper PRT, Schreckenbach G, Seldenthuis JS, Seth M, Snijders JG, Sola M, Swart M, Swerhone D, te Velde G, Vernooijs P, Versluis L, Visscheri L, Visser O, Wang F, Wesolowski TA, van Wezenbeek EM, Wiesenekker G, Wolff SK, Woo TK, Yakovlev AL. ADF2010, SCM, Theoretical Chemistry, Vrije Universiteit, Amsterdam, The Netherlands, <http://www.scm.com>
53. Vosko SH, Wilk L, Nusair M (1980) *Can J Phys* 58:1200
54. Perdew JP (1986) *Phys Rev B* 33:8822
55. Becke AD (1988) *Phys Rev A* 38:3098
56. van Leeuwen R, van Lenthe E, Baerends EJ, Snijders JG (1994) *J Chem Phys* 101:1272
57. Christiansen O, Koch H, Jørgensen P (1995) *Chem Phys Lett* 243:409
58. Hättig C, Weigend F (2000) *J Chem Phys* 113:5154
59. Hättig C, Köhn A (2002) *J Chem Phys* 117:6939
60. Becke AD (1993) *J Chem Phys* 98:5648
61. Lee C, Yang W, Parr RG (1988) *Phys Rev B* 37:785
62. Weigend F, Häser M, Patzelt H, Ahlrichs R (1998) *Chem Phys Lett* 294:143
63. Furche F, Ahlrichs R (2002) *J Chem Phys* 117:7433
64. Furche F, Ahlrichs R (2004) *J Chem Phys* 121:12772
65. Kohout M (2005) Programs DGrid and Basin. <http://www.scm.com/News/DGrid.html>
66. Kohout M (2004) *Int J Quant Chem* 97:651
67. Wolinski K, Hinton JF, Pulay P (1990) *J Am Chem Soc* 112:8251
68. Häser M, Ahlrichs R, Baron HP, Weis P, Horn H (1992) *Theor Chim Acta* 83:455
69. Kollwitz M, Häser M, Gauss J (1998) *J Chem Phys* 108:8295
70. Ahlrichs R, May K (2000) *Phys Chem Chem Phys* 2:943
71. Li S, Dixon DA (2007) *J Phys Chem A* 111:11093
72. Pyykkö P, Riedel S, Patzschke M (2005) *Chem Eur J* 11:3511
73. Jusélius J, Sundholm D (2001) *Phys Chem Chem Phys* 3:2433
74. Chen Z, Wannere CS, Corminboeuf C, Puchta R, von Ragué Schleyer P (2005) *Chem Rev* 105:3842
75. Pyykkö P, Desclaux JP (1978) *Chem Phys* 34:261
76. Sundholm D, Pyykkö P, Laaksonen L (1985) *Finn Chem Lett* 51–55
77. El-Issa BD, Pyykkö P, Zanati HM (1991) *Inorg Chem* 30:2781
78. Pyykkö P, Tamm T (1997) *J Phys Chem A* 101:8107
79. Pyykkö P, Runeberg N (2002) *Angew Chem Int Ed* 41:2174
80. Gagliardi L, Pyykkö P (2004) *Phys Chem Chem Phys* 6:2904. doi:[10.1039/b404255g](https://doi.org/10.1039/b404255g)
81. Autschbach J, Hess BA, Johansson MP, Neugebauer J, Patzschke M, Pyykkö P, Reiher M, Sundholm D (2004) *Phys Chem Chem Phys* 6:11
82. Manninen K, Pyykkö P, Häkkinen H (2005) *Phys Chem Chem Phys* 7:2208
83. Johansson MP, Pyykkö P (2010) *Chem Commun* 46:3762. doi:[10.1039/c0cc0045k](https://doi.org/10.1039/c0cc0045k)
84. Laaksonen L (1992) *J Mol Graph* 10:33
85. Bergman DL, Laaksonen L, Laaksonen A (1997) *J Mol Graph Model* 15:301